

Cite this: *RSC Adv.*, 2018, 8, 41491

Supported binary CuO_x -Pt catalysts with high activity and thermal stability for the combustion of NH_3 as a carbon-free energy source†

Saaya Kiritoshi,^a Takeshi Iwasa,^b Kento Araki,^a Yusuke Kawabata,^a Tetsuya Taketsugu,^b Satoshi Hinokuma^{b,*ac} and Masato Machida^a

Recently, NH_3 has been thought to be a renewable and carbon-free energy source. The use of NH_3 fuel, however, is hindered by its high ignition temperature and $\text{N}_2\text{O}/\text{NO}$ production. To overcome these issues, in this study, the combustion of NH_3 over copper oxide (CuO_x) and platinum (Pt) catalysts supported on aluminium silicates ($3\text{Al}_2\text{O}_3 \cdot 2\text{SiO}_2$), aluminium oxides (Al_2O_3), and silicon oxides (SiO_2) were compared. To achieve high catalytic activity for the combustion of NH_3 and high selectivity for N_2 (or low selectivity for $\text{N}_2\text{O}/\text{NO}$), conditions for the preparation of impregnated binary catalysts were optimised. With respect to the binary catalysts, sequentially impregnated $\text{CuO}_x/\text{Pt}/\text{Al}_2\text{O}_3$ exhibited relatively higher activity, N_2 selectivity, and thermal stability. From XRD and XAFS analyses, CuO_x and Pt in $\text{CuO}_x/\text{Pt}/\text{Al}_2\text{O}_3$ were present as CuAl_2O_4 and metallic Pt, respectively. Given that the combustion activity was closely associated with the Pt nanoparticle size, which was estimated from the Scherrer equation and the pulsed CO technique, highly dispersed Pt nanoparticles were crucial for the low-temperature light-off of NH_3 . For single and binary catalysts, although NH (imide) deformation modes as a key species for N_2O production were detected by *in situ* FTIR spectral analysis, the band intensity of $\text{CuO}_x/\text{Pt}/\text{Al}_2\text{O}_3$ was less than those of $\text{CuO}_x/\text{Al}_2\text{O}_3$ and $\text{Pt}/\text{Al}_2\text{O}_3$. Therefore, $\text{CuO}_x/\text{Pt}/\text{Al}_2\text{O}_3$ exhibits high selectivity for N_2 in NH_3 combustion.

Received 25th September 2018
Accepted 27th November 2018

DOI: 10.1039/c8ra07969b

rsc.li/rsc-advances

Introduction

Recent studies have reportedly considered NH_3 to serve not only as a H_2 carrier material but also as a renewable, carbon-free energy source because of its high energy density (3160 W h L^{-1}) and negligible thermal NO_x emission.¹ Currently, NH_3 is industrially produced at a high pressure using N_2 (produced from air) and H_2 (produced from natural gas) by employing the Haber-Bosch process, which consumes a large amount of energy. However, the energy and costs associated with H_2 production and natural gas is 70–90% of that required for NH_3 production.² Therefore, the low energy and costs that are associated with H_2

production along with the fact that it is a renewable energy source should be emphasised to ensure that the society utilises H_2 along with NH_3 . As a proof-of-concept for using NH_3 as a fuel, an NH_3 -fuelled micro-gas turbine has been employed to demonstrate the potential of NH_3 -fired power plants at the Fukushima Renewable Energy Institute in Japan, as well as an NH_3 -fuelled industrial furnace.³ Compared to fossil fuels, however, NH_3 exhibits disadvantages of a high ignition temperature, low combustion rate, and $\text{N}_2\text{O}/\text{NO}_x$ production. Therefore, to overcome these issues, it is imperative to develop a novel NH_3 combustion system. First, a catalytic NH_3 combustion system, which decreases the ignition temperature and $\text{N}_2\text{O}/\text{NO}_x$ emissions, was developed. Previously, our group has successfully developed a catalytic NH_3 combustion system and novel catalysts exhibiting high activity, N_2 selectivity, and thermal stability.⁴ For example, copper oxides (CuO_x) supported on Al_2O_3 -based composite oxide materials (such as $10\text{Al}_2\text{O}_3 \cdot 2\text{B}_2\text{O}_3$ and $3\text{Al}_2\text{O}_3 \cdot 2\text{SiO}_2$) exhibit high N_2 selectivity and thermal stability, whereas binary CuO_x and silver (Ag) supported on Al_2O_3 exhibit high activity and N_2 selectivity.⁴ However, the former catalyst exhibits a low activity (ignition temperature at $\sim 300^\circ\text{C}$), while the latter catalyst exhibits low thermal stability (deactivation temperature at $\sim 900^\circ\text{C}$ likely because of the low melting point of Ag).⁴ Therefore, it is imperative to develop catalysts to exhibit high activities and thermal stabilities for NH_3 combustion.

^aField of Environmental Chemistry and Materials, Division of Materials Science and Chemistry, Faculty of Advanced Science and Technology, Kumamoto University, 2-39-1 Kurokami, Chuo-ku, Kumamoto 860-8555, Japan. E-mail: hinokuma@kumamoto-u.ac.jp; Tel: +81-96-342-3653

^bDepartment of Chemistry, Faculty of Science, Hokkaido University, Sapporo 060-0810, Japan

^cInternational Research Organization for Advanced Science and Technology, Kumamoto University, Japan

† Electronic supplementary information (ESI) available: Calculation formulae, calculated thermodynamic Pt-PtO_x phase equilibrium, XRD patterns, HAADF-STEM/EDX mapping images, product selectivities for the NH_3 -O₂ and NH_3 -NO-O₂ reactions, relationship between NH_3 combustion activity and Pt particle size, NH_3 - and NO-TPD profiles. See DOI: 10.1039/c8ra07969b



On the other hand, binary systems comprising supported $\text{CuO}_x\text{-Ag}$,⁵ $\text{CuO}_x\text{-Pt}$,⁶ $\text{CuO}_x\text{-Au}$,⁷ $\text{CuO}_x\text{-CeO}_2$ ⁸ and $\text{-Li}_2\text{O}_3$ ⁸ catalysts exhibiting a high performance for the selective catalytic oxidation of NH_3 ($\text{NH}_3\text{-SCO}$) have been previously reported. In particular, $\text{CuO}_x\text{-Pt}$ systems are expected to exhibit high thermal stability because of the high melting point of Pt (~ 1770 °C). Recently, Sun *et al.* have synthesised impregnated $\text{CuO}_x\text{-Pt/ZSM-5}$ catalysts and reported that CuO_x on Pt species can lead to higher $\text{NH}_3\text{-SCO}$ performance compared to single catalysts.⁶ On the other hand, Jabłońska has synthesised Al_2O_3 -, TiO_2 -, and ZrO_2 -supported $\text{CuO}_x\text{-Pt}$, -Pd and -Rh catalysts⁶ and found that the supported $\text{CuO}_x\text{-Pt}$ catalyst exhibits high activity and N_2 selectivity for $\text{NH}_3\text{-SCO}$. However, in these studies, NH_3 is considered to cause air pollution; therefore, the thermal stability is investigated at temperatures of less than 900 °C.

In this study, supported binary $\text{CuO}_x\text{-Pt}$ catalysts were synthesised, and their catalytic properties for the combustion of NH_3 (as an energy source) at high reaction temperatures were examined. To achieve high catalytic activity for the combustion of NH_3 , N_2 (low $\text{N}_2\text{O/NO}$) selectivity and thermal stability, preparation conditions for impregnated binary catalysts were optimised. Moreover, the relationship between the local structure and catalytic properties for the combustion of NH_3 over supported $\text{CuO}_x\text{-Pt}$ catalysts was discussed.

Experimental

Catalyst preparation

$3\text{Al}_2\text{O}_3 \cdot 2\text{SiO}_2$ (3A2S) of the catalyst support material was prepared by using an alkoxide method. According to previous studies,^{4,9} $\text{Si}(\text{OC}_2\text{H}_5)_4$ (TEOS, Wako Pure Chemicals) was first dissolved in $\text{C}_2\text{H}_5\text{OH}$ (Wako Pure Chemicals) at a concentration of 1 M at room temperature (RT). Second, after the addition of H_2O and HCl (Wako Pure Chemicals), the solution was stirred at 70 °C for 5 h, and a Si solution was prepared. Third, the alcohol was dehydrated. The H_2O and HCl concentrations were $\text{H}_2\text{O/TEOS} = 2$ (mol mol^{-1}) and $\text{HCl/TEOS} = 0.1$ (mol mol^{-1}), respectively. Next, $\text{Al}[\text{OCH}(\text{CH}_3)_2]_3$ (AIP, Sigma-Aldrich) was subjected to reflux conditions and dissolved in $(\text{CH}_3)_2\text{CHCH}_2\text{OH}$ (Nacalai Tesque) to prepare an Al solution. The precursor solution was prepared by mixing the Al and Si solutions in a volume ratio of 3 : 2 at RT. H_2O was added, and the solution was stirred for 1 h to prepare the precursor solution. The precursor sols were dried at 110 °C for 48 h, affording xerogel precursor powders. These powders were pulverised and calcined at 600 °C for 3 h and finally at 1200 °C for 5 h in air. In addition, $\alpha\text{-Al}_2\text{O}_3$ (Wako Pure Chemicals), $\gamma\text{-Al}_2\text{O}_3$ (JRC-ALO-8, Catalysis Society of Japan), SiO_2 (JRC-SIO-10, Catalysis Society of Japan), and CuO (Wako Pure Chemicals) were used as support materials.

Single and binary supported CuO_x (CuO loading of 6 wt%) and/or Pt (Pt loading of 2 wt%) catalysts were prepared by the co-impregnation ($\text{CuO}_x\text{-Pt}$) of an aqueous solution of $\text{Cu}(\text{NO}_3)_2$ (Wako Pure Chemicals) and $[\text{Pt}(\text{NH}_3)_2(\text{NO}_3)_2]$ (Tanaka Kikinzoku Kogyo), followed by drying and calcination at 600 °C for 3 h in air. In addition, the sequentially impregnated binary catalysts, *i.e.* Pt and subsequent CuO_x (CuO_x/Pt) and/or CuO_x and

subsequent Pt (Pt/CuO_x), were synthesised in a similar fashion. As $\text{CuO}_x/\text{Pt/Al}_2\text{O}_3$ exhibited a high catalytic activity for the combustion of NH_3 , physically mixed catalysts ($\text{CuO} + \text{Pt/Al}_2\text{O}_3$, $\text{CuAl}_2\text{O}_4 + \text{Pt/Al}_2\text{O}_3$, and $\text{CuO}_x/\text{Al}_2\text{O}_3 + \text{Pt/Al}_2\text{O}_3$) with the same composition ratios were also prepared. To evaluate their thermal stabilities and catalytic properties, the as-prepared catalysts were subjected to thermal aging at 900 °C for 100 h in air and/or at 1000 °C for 5 h in air.

Characterisation

Powder X-ray diffraction (XRD) patterns were recorded using monochromatic $\text{Cu K}\alpha$ radiation (30 kV, 20 mA, Multiflex, Rigaku). The average size of the Pt particles was calculated by the XRD line broadening method by using the Scherrer equation.¹⁰ The chemical composition was determined by X-ray fluorescence (XRF; EDXL-300, Rigaku) measurements. High-angle annular dark-field scanning transmission electron microscopy (HAADF-STEM) and energy-dispersive X-ray spectroscopy (EDS) mapping images were recorded on a JEM-ARM200CF (JEOL) system. Brunauer-Emmett-Teller (BET) surface area (S_{BET}) values were calculated from the N_2 adsorption isotherms, which were recorded at -196 °C (Belsorp, Bel Japan, Inc.). Pt dispersion and particle size were determined by the pulsed CO technique (BELCAT-B, BEL Japan, Inc.) at 50 °C after O_2 oxidation and subsequent H_2 reduction at 400 °C according to previous studies.¹¹ Pt dispersion and particle size were calculated by assuming hemispherical particles with the stoichiometric adsorption of CO on Pt at a CO : Pt ratio of 1 : 1. Cu K-edge and Pt $\text{L}_{3\text{-edge}}$ X-ray absorption fine structure (XAFS) spectral analyses were carried out at BL9A of PF and BL01B1 of SPring-8. XAFS spectra were recorded in the transmission mode at RT using an ionisation chamber filled with N_2 for the incident beam, another chamber filled with 75% N_2/Ar for the Cu K-edge and 50% N_2/Ar for Pt $\text{L}_{3\text{-edge}}$ for the transmitted beam, and a $\text{Si}(111)$ double-crystal monochromator. Reference samples (*e.g.* Cu_2O , CuO , CuAl_2O_4 , and PtO_2) were mixed with boron nitride (BN) powder to achieve an appropriate absorbance at the edge energy, whereas the catalysts were used without mixing with BN. XAFS data were processed using the IFEFFIT software package (Athena and Artemis).

Catalytic NH_3 combustion tests

The catalytic combustion of NH_3 was performed in a flow reactor at atmospheric pressure. Catalysts (10–20 mesh, <0.3 mm thickness, 50 mg) were fixed in a quartz tube (OD: 6 mm, ID: 4 mm) with quartz wool at both ends of the catalyst bed. The temperature dependence of the catalytic activity was evaluated by heating the catalyst bed from RT to 900 °C at a constant rate of 10 °C min^{-1} while a gas mixture containing 1.0% NH_3 , 1.5% O_2 and He balance at 100 cm^3 min^{-1} ($W/F = 5.0 \times 10^{-4}$ g min cm^{-3}) was supplied. The O_2 excess ratio for NH_3 combustion was expressed as $\lambda = (p_{\text{O}_2}/p_{\text{NH}_3})_{\text{exp}} / (p_{\text{O}_2}/p_{\text{NH}_3})_{\text{stoichiom.}}$, where p denotes pressure. The $\text{NH}_3/\text{N}_2\text{O/NO}$, N_2 and NO_2 gas concentrations were analysed using a nondispersive infrared gas analyser (VA-3011, Horiba), chromatography (GC-8A, Shimadzu) and chemiluminescence (NOA-7000,



Shimadzu) measurements. The ESI[†] provides the calculation formulae used to determine the concentration ratios.

In situ Fourier transform infrared (FTIR) spectra were recorded on a Nicolet 6700 spectrometer using a diffuse-reflectance reaction cell with a BaF₂ window connected to a gas supply and a heating system to enable measurements at atmospheric pressure. First, the catalysts were preheated *in situ* in flowing He at 400 °C for 30 min prior to each experiment. After pre-treatment, the temperature of the catalyst was decreased to 200 °C, followed by the subsequent purging of the cell with He and then filling with 0.3% NH₃/He mixed gas. Finally, FTIR spectra were recorded while the catalysts were maintained under a stream of NH₃/He.

Computational details

Spin-restricted density functional theory (DFT) computations were carried out for NH₃/Pt_x ($x = 13$ and/or 20) at the M06 level using the def-SV(P) basis sets, with the 60-electron relativistic effective core potential for Pt, as implemented in TURBOMOLE under the resolution of the identity approximation.¹² The model clusters of Pt₁₃ with *I*_h symmetry and Pt₂₀ with *T*_d symmetry having four (111) faces were locally optimised until imaginary frequencies were removed. One atop geometry for NH₃-Pt₁₃ and three initial geometries for NH₃-Pt₂₀ were considered, *i.e.* atop the (111) face; bridge-to-edge site; and atop the vertex site, respectively. These geometries were optimised until no imaginary frequencies were observed. The adsorption energy of NH₃ on Pt_x was estimated as $E_{\text{ads}} = E(\text{NH}_3) + E(\text{Pt}_x) - E(\text{NH}_3\text{-Pt}_x)$, where $E(A)$ denotes the electronic energy of species *A*.

Results & discussion

Local structures of supported CuO_x and Pt catalysts

Fig. 1 shows the XRD patterns of sequentially impregnated binary (CuO_x/Pt) catalysts, because CuO_x/Pt/Al₂O₃ exhibited

higher activity, N₂ (lower N₂O/NO) selectivity, and thermal stability for the combustion of NH₃ compared to all binary catalysts before and after thermal ageing at 900 °C (Table 1). ESI[†] shows the XRD patterns of the other catalysts. The XRD patterns of as-prepared CuO_x/Pt/3A2S and CuO_x/Pt/SiO₂ before and after aging revealed peaks corresponding to CuO, whereas peaks corresponding to CuAl₂O₄ were observed for CuO_x/Pt/3A2S and CuO_x/Pt/Al₂O₃ (900 °C), possibly related to the solid-state reaction between γ -Al₂O₃ and CuO_x. Diffraction peaks for Cu species were not observed for as-prepared CuO_x/Pt/Al₂O₃, possibly related to the high dispersion of CuO_x. The Al₂O₃ phase for the binary catalysts was transformed from γ to α , and the diffraction peaks for Pt became sharper after thermal aging at temperatures of higher than 900 °C. Therefore, the growth of particles and sintering of Al₂O₃ and Pt are induced by thermal aging. Indeed, the Pt particle sizes calculated by the Scherrer equation increased with the aging temperature (Table 1). On the other hand, as peaks corresponding to CuO were observed for the binary catalysts prepared using α -Al₂O₃ (CuO_x/Pt/ α -Al₂O₃) before and after aging, it was possibly difficult to form CuAl₂O₄ from the solid-state reaction between α -Al₂O₃ and CuO_x (ESI[†]).

Fig. 2 shows the normalised Cu K-edge X-ray absorption near-edge structure (XANES) spectra and *k*-space extended X-ray absorption fine structure (EXAFS) oscillations of the catalysts and the three reference compounds (Cu₂O, CuO and CuAl₂O₄, respectively). Cu K-edge XANES spectra and *k*-space EXAFS oscillations of CuO_x/Pt/3A2S (900 °C) and CuO_x/Pt/Al₂O₃ before and after thermal aging at 900 °C were similar to those of CuAl₂O₄, whereas those of CuO_x/Pt/3A2S and CuO_x/Pt/SiO₂ before and after thermal aging at 900 °C were similar to those of CuO. In the XANES spectra of CuO_x/Pt/3A2S and CuO_x/Pt/SiO₂ before and after aging, the pre-edge (at ~8985 eV, corresponding to Cu²⁺ 1s → 4p + ligand and Cu²⁺ 1s → Cu²⁺ charge-transfer excitation)¹³ for CuO was observed. XAFS analyses were consistent with the XRD patterns of the catalysts. The Pt L₃-edge XAFS profiles of the catalysts and two references (*i.e.* Pt foil and PtO₂, respectively) are also depicted in Fig. 3. For as-prepared CuO_x/Pt/Al₂O₃, the XANES profile was slightly similar to that observed for PtO₂. According to the calculated thermodynamic Pt-PtO_x phase equilibrium (ESI[†]), PtO₂ and metallic Pt exhibited thermodynamic stability at RT and 600 °C, respectively. Therefore, Pt nanoparticles (especially, their surfaces) in CuO_x/Pt/Al₂O₃ are thought to be oxidised during the cooling process of calcination. By contrast, the XANES profiles of the other catalysts were similar to that of Pt foil (metallic Pt) as against the calculated phase equilibrium. This disagreement is supposedly caused by the calcination and/or thermal aging-induced sintering of metallic Pt nanoparticles in these catalysts; hence, the bulk metallic Pt particles are stable at RT.

Next, HAADF-STEM and EDS mapping images of sequentially impregnated CuO_x/Pt/Al₂O₃ (900 °C) were recorded (Fig. 4). From the HAADF-STEM image, dispersed nanoparticles with a bright contrast supported on Al₂O₃ particles (blue for Al) were observed, and the EDS mapping images revealed the presence of Pt (red). On the other hand, for the CuO_x species of CuO_x/Pt/Al₂O₃ (900 °C), the EDS mapping images revealed the presence of CuO_x aggregates (green). However, because the

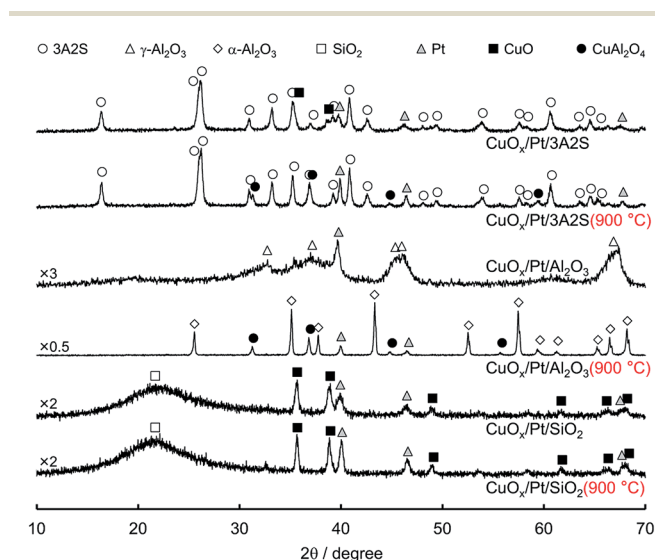


Fig. 1 XRD patterns of sequentially impregnated catalysts before and after thermal aging 900 °C for 100 h in air.



Table 1 Catalytic properties of supported catalysts before and after thermal aging at 900 °C for 100 h in air

Catalyst	Phase	$T_{10}^a/^\circ\text{C}$	$T_{90}^a/^\circ\text{C}$	Selectivity at $T_{90}^a/^\circ\text{C}$			$S_{\text{BET}}/\text{m}^2\text{g}^{-1}$	Pt particle size/nm		Desorbed gas ^d /μmol m ⁻²	
				N ₂	N ₂ O	NO		^b XRD	^c Pulsed CO	NH ₃	NO
CuO _x /Pt/3A2S	CuO/Pt/3A2S	210	356	90	8	2	32		18		
CuO _x /Pt/3A2S (900 °C)	CuAl ₂ O ₄ /Pt/3A2S	203	344	89	10	1	27		50		
CuO _x /Al ₂ O ₃	CuAl ₂ O ₄ /γ-Al ₂ O ₃	303	476	92	6	2	149			1.3	0.050
CuO _x /Al ₂ O ₃ (900 °C)	CuAl ₂ O ₄ /α, γ-Al ₂ O ₃	295	450	91	8	1	102			0.4	0.063
Pt/Al ₂ O ₃	Pt/γ-Al ₂ O ₃	188	289	81	19	<1	156	11	11	0.6	0.051
Pt/Al ₂ O ₃ (900 °C)	Pt/γ, θ-Al ₂ O ₃	213	266	87	12	<1	99	31	^e n. d.	2.0	0.140
CuO _x /Pt/Al ₂ O ₃	CuAl ₂ O ₄ /Pt/γ-Al ₂ O ₃	189	278	86	13	<1	139	15	5	1.6	0.064
CuO _x /Pt/Al ₂ O ₃ (900 °C)	CuAl ₂ O ₄ /Pt/α-Al ₂ O ₃	220	339	86	13	1	14	33	176	1.5	0.444
CuO _x /Pt/SiO ₂	CuO/Pt/SiO ₂	234	316	93	7	<1	182	13	^e n. d.		
CuO _x /Pt/SiO ₂ (900 °C)	CuO/Pt/SiO ₂	301	456	96	<1	3	81	24	^e n. d.		

^a Temperature at which NH₃ conversion reached 10% and 90%. ^b Calculated from XRD line broadening method. ^c Calculated from pulsed CO chemisorption. ^d Estimated by NH₃- and NO-TPD ranging from 50 °C to 500 °C. ^e The amount of CO chemisorption was not detected (n. d.).

overlap of the fluorescence lines of Pt-L and Cu-K, as denoted by the solid arrows in the overlaid image, a physical proximity between Pt and CuO_x nanoparticles in CuO_x/Pt/Al₂O₃ was supposed after aging at 900 °C. On the other hand, Pt particles with sizes larger than 200 nm were clearly observed for CuO_x/Pt/SiO₂ (900 °C) (ESI†).

Combustion properties of supported CuO_x and Pt catalysts

Fig. 5 shows the comparison of the temperature dependence on the selectivities of products obtained over supported CuO_x/Pt, CuO_x/Al₂O₃ and Pt/Al₂O₃ before and after thermal aging at 900 °C under O₂ excess conditions ($\lambda = 2$). ESI† shows those of the other catalysts. With respect to the supported CuO_x/Pt catalysts before and after aging, CuO_x/Pt/Al₂O₃ exhibited a comparatively higher catalytic NH₃ combustion activity and N₂ (lower N₂O/NO) selectivity. For CuO_x/Pt/Al₂O₃ and Pt/Al₂O₃ before and after aging, the light-off curves for NH₃ were obtained at ~200 °C, whereas CuO_x/Al₂O₃ exhibited lower catalytic activity (T_{10} : ~300 °C). On the other hand, before and after aging, CuO_x/Pt/Al₂O₃ and CuO_x/Al₂O₃ exhibited lower NO selectivity compared to Pt/Al₂O₃ although NO selectivities for all catalysts were observed after the NH₃ conversion reached ~90%. In contrast, the selectivity of N₂O over the catalysts before and after aging increased in the order of CuO_x/Al₂O₃ < CuO_x/Pt/Al₂O₃ < Pt/Al₂O₃. Finally, CuO_x/Pt/Al₂O₃ exhibited higher N₂ selectivity. Therefore, binary CuO_x/Pt/Al₂O₃ renders synergistic effects of Pt (enhancing the NH₃-O₂ reaction) and CuO_x (increasing N₂ selectivity). To investigate the low NO selectivity of CuO_x/Pt/Al₂O₃ and CuO_x/Al₂O₃, an NH₃-NO-O₂ reaction test (0.8% NH₃, 0.2% NO, 1.4% O₂, He balance) was also performed (shown in ESI†). For the NH₃-NO reaction, CuO_x/Pt/Al₂O₃ also exhibited higher activity compared to CuO_x/Al₂O₃ and Pt/Al₂O₃. NH₃ was supposedly consumed not only by O₂ but also by NO, which was formed as an intermediate during the light-off of NH₃. However, the selectivity of N₂O for the NH₃-NO-O₂ reaction over CuO_x/Pt/Al₂O₃ was higher than that for the

combustion of NH₃ (Fig. 5), indicating that the N₂O is produced from the NH₃-NO reaction.

For N₂O production, on the other hand, according to the kinetic model for NH₃ oxidation, the elementary reaction of NH (imide) + NO → N₂O + H exhibited high sensitivity for N₂O production.¹⁴ Moreover, for catalytic NH₃ oxidation and NH₃-NO reactions, NH was also regarded as a key species for N₂O production.¹⁵ Therefore, to verify the adsorption of NH on the catalysts, *in situ* FTIR spectra of NH₃ adsorbed on the catalysts before and after aging were recorded at 200 °C (Fig. 6); this temperature is the approximate initiation temperature for NH₃ combustion (Fig. 5). As has been reported previously,¹⁵ FTIR bands were observed at 1250 and 1625 cm⁻¹, corresponding to the deformation modes of NH₃ adsorbed on Lewis acid sites, for all catalysts. Moreover, for Pt/Al₂O₃ and CuO_x/Pt/Al₂O₃, a set of bands were slightly observed at 1395 and 1695 cm⁻¹, corresponding to the asymmetric and symmetric bending vibrations of NH₃ species on the Brønsted acid sites. Although the single band at 1458 cm⁻¹ corresponding to the NH (considered as a species for N₂O production) deformation modes was observed for all catalysts, the band intensity for CuO_x/Pt/Al₂O₃ was less than that for Pt/Al₂O₃. As CuO_x/Pt/Al₂O₃ prevented the production of NO from the combustion of NH₃ and the dissociative adsorption of NH₃, the catalyst finally achieved high N₂ selectivity.

Catalytic properties of supported CuO_x and/or Pt

Table 1 summarises the catalytic properties of supported CuO_x/Pt, CuO_x/Al₂O₃ and Pt/Al₂O₃ before and after thermal aging at 900 °C, and ESI† shows those of the other catalysts. Catalytic activity was expressed in terms of the light-off temperature at which 10% conversion of NH₃ was achieved (T_{10}), and the product selectivities were evaluated at the reaction temperature at which 90% NH₃ conversion was achieved (T_{90}). ESI† shows the temperature dependence of the product selectivities for the combustion of NH₃ over the catalysts. For single catalysts supported on each material (*i.e.* 3A2S, Al₂O₃ and SiO₂), supported



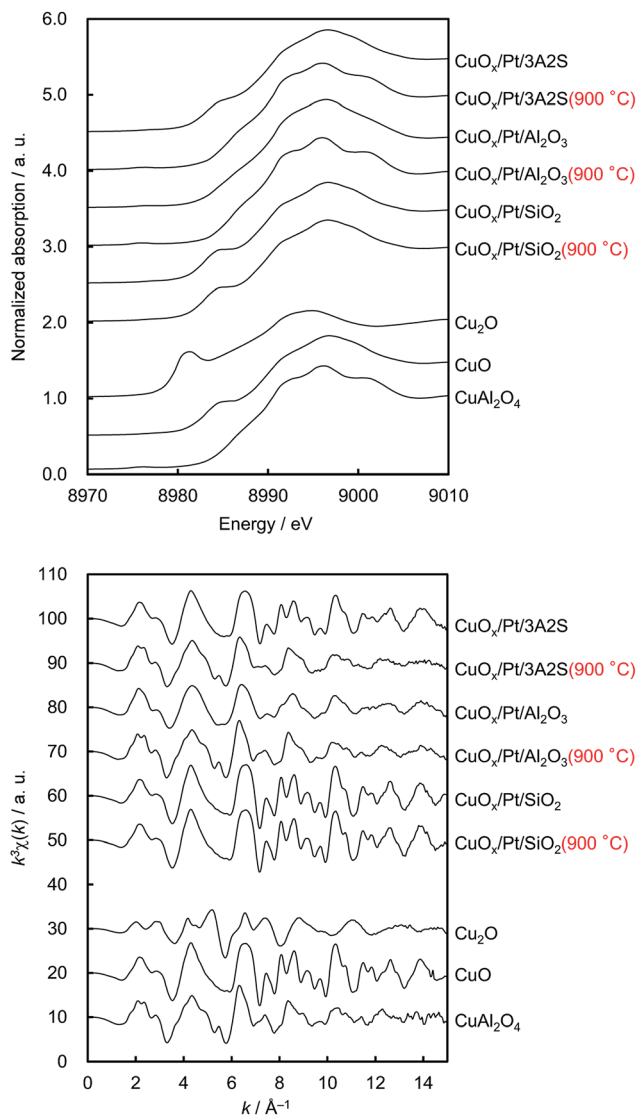


Fig. 2 Cu K-edge (upper) normalised XANES spectra and (lower) EXAFS oscillations of sequentially impregnated catalysts before and after thermal aging and three references (*i.e.* Cu_2O , CuO , and CuAl_2O_4 , respectively).

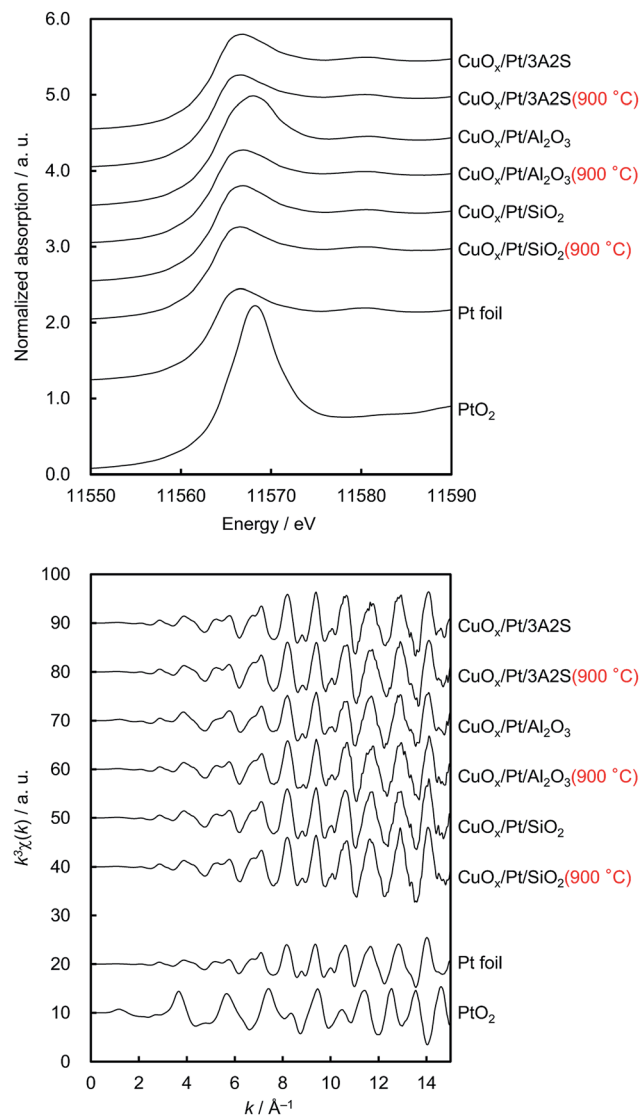


Fig. 3 Pt L_{3} -edge (upper) normalised XANES spectra and (lower) EXAFS oscillations of sequentially impregnated catalysts before and after thermal aging and two references (*i.e.* Pt foil and PtO_2 , respectively).

CuO_x exhibited low activity and $\text{N}_2\text{O}/\text{NO}$ selectivities, whereas supported Pt exhibited high activity and $\text{N}_2\text{O}/\text{NO}$ selectivity (ESI^\dagger). On the other hand, binary supported catalysts exhibited the same high activity as the single supported Pt, albeit a slightly lower $\text{N}_2\text{O}/\text{NO}$ selectivity. As the combustion activity was closely associated with the Pt particle size, which was calculated by the Scherrer equation (plot shown in the ESI^\dagger), highly dispersed Pt nanoparticles supposedly played a key role in the low-temperature light-off of NH_3 . In this study, for pulsed CO chemisorption, it is expected that CO is adsorbed not only on Pt but also on CuO_x in case of binary system catalysts.¹⁶ Therefore, the correlation between the NH_3 combustion activity (T_{10}) and the Pt particle size can be estimated using the XRD line broadening method by employing the Scherrer equation.

To elucidate the correlation between the activity and size of Pt nanoparticles, the adsorption energy (E_{ads}) between NH_3 and Pt_{13} and/or Pt_{20} clusters (Pt–N) were estimated by DFT computations (Fig. 7). Compared with the Pt–N E_{ads} of the vertex for the Pt_{20} (larger) cluster, that of the vertex for the Pt_{13} (smaller) cluster was higher, indicating that NH_3 preferentially adsorbs on highly dispersed Pt nanoparticles as well as coordinatively unsaturated (cus) Pt atoms. Indeed, for the Pt_{20} cluster, the Pt–N E_{ads} of three initial geometries (see inset in Fig. 7) increased in the order of atop < edge < vertex. Moreover, the bond distance of N–H in NH_3 adsorbed on Pt_{13} was longer than that on Pt_{20} , suggesting that cus Pt exhibits high activity for the dissociation of the N–H bond in adsorbed NH_3 . Compared with the activity of binary CuO_x –Pt catalysts prepared by co-impregnation, those of the sequentially impregnated CuO_x /Pt catalysts were higher



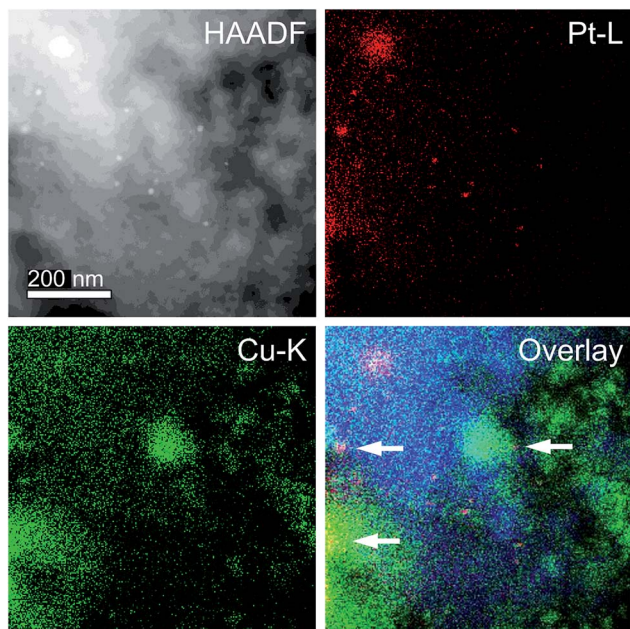


Fig. 4 HAADF-STEM image and EDS mapping analysis of $\text{CuO}_x/\text{Pt}/\text{Al}_2\text{O}_3$ (900 °C). Red, green, and blue points denote the Pt-L, Cu-K, and Al-K fluorescence lines, respectively.

probably because Pt nanoparticles can be highly dispersed onto each support material without inhibition from the presence of CuO_x .

Among the CuO_x/Pt catalysts supported on various support materials, $\text{CuO}_x/\text{Pt}/\text{Al}_2\text{O}_3$ exhibited a relatively higher activity, N_2 selectivity, and thermal stability (Table 1). However, a significant decrease in S_{BET} was observed for $\text{CuO}_x/\text{Pt}/\text{Al}_2\text{O}_3$ (900 °C) ($139 \rightarrow 14 \text{ m}^2 \text{ g}^{-1}$) in comparison with that observed for $\text{CuO}_x/\text{Al}_2\text{O}_3$ (900 °C) and $\text{Pt}/\text{Al}_2\text{O}_3$ (900 °C). For this reason, first, it is considered that the significant decrease in specific surface area can be attributed to the phase transition of ($\gamma \rightarrow \alpha$) Al_2O_3 as well as thermal aging at 900 °C. However, in case of only $\gamma\text{-Al}_2\text{O}_3$, the phase transformation to $\alpha\text{-Al}_2\text{O}_3$ was observed at approximately 1200 °C.¹⁷ Next, however, according to a previous report related to the effects of divalent cation additives on the phase transition of ($\gamma \rightarrow \alpha$) Al_2O_3 , the additive Cu^{2+} species that coexist with $\gamma\text{-Al}_2\text{O}_3$ accelerates its phase transition to $\alpha\text{-Al}_2\text{O}_3$ at a low temperature of 1200 °C, which can be attributed to the fact that CuAl_2O_4 is formed at a temperature of lower than 1200 °C.¹⁸ Indeed, in this study, $\alpha\text{-Al}_2\text{O}_3$ was observed in $\text{CuO}_x/\text{Al}_2\text{O}_3$ after thermal aging at 900 °C (Table 1). Finally, it is probable that the additive and co-existing Pt also accelerates the formation of CuAl_2O_4 as well as the phase transition to $\alpha\text{-Al}_2\text{O}_3$. Although no concrete data are available, a similar significant decrease of the specific surface area could be observed in both Cu–Al–O and Cu–Pt–Al–O system catalysts after thermal aging occurred at 1000 °C.¹⁹

Notably, the high performance for $\text{CuO}_x/\text{Pt}/\text{Al}_2\text{O}_3$ was maintained after thermal aging at 1000 °C despite the phase transition ($\gamma \rightarrow \alpha$) and decrease in the surface area. On the other hand, CuO_x/Pt supported on $\alpha\text{-Al}_2\text{O}_3$ exhibited slightly higher N_2/NO

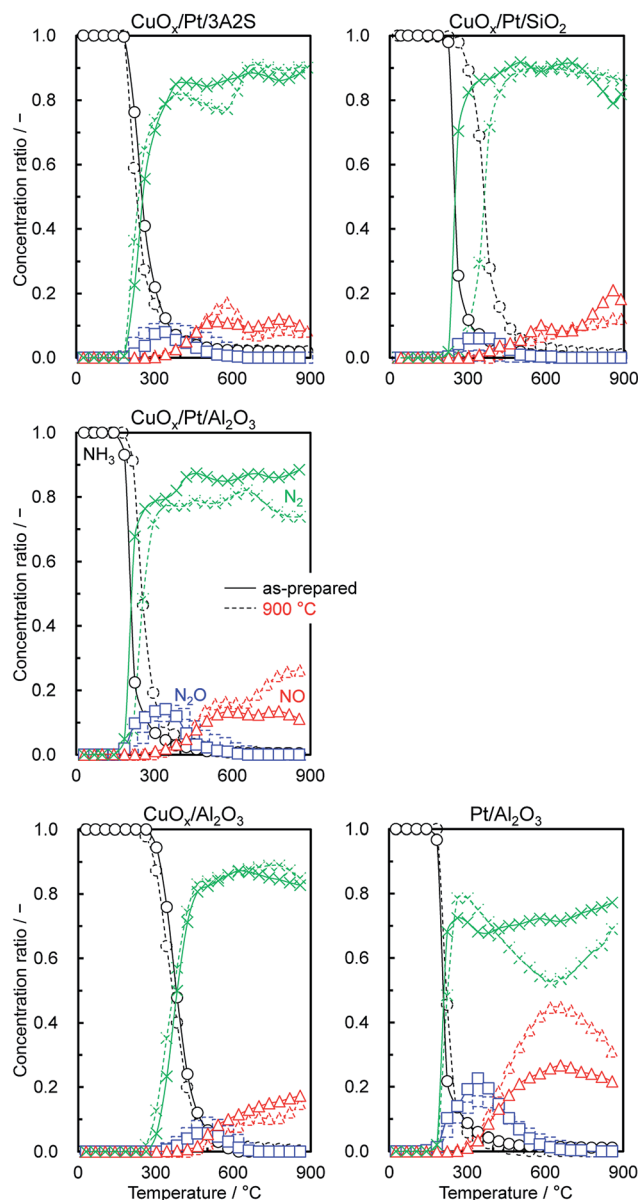


Fig. 5 Product selectivities for the catalytic combustion of NH_3 ($\text{NH}_3\text{-O}_2$) over catalysts before and after thermal aging in air at 900 °C for 100 h. Reaction conditions: 1.0% NH_3 , 1.5% O_2 , $\lambda = 2$, He balance, $W/F = 5.0 \times 10^{-4} \text{ g min cm}^{-3}$.

selectivities compared to $\text{CuO}_x/\text{Pt}/\text{Al}_2\text{O}_3$ (using $\gamma\text{-Al}_2\text{O}_3$), the results of which can be explained from the difference in the CuO_x phase of CuO in $\text{CuO}_x/\text{Pt}/\alpha\text{-Al}_2\text{O}_3$ and CuAl_2O_4 in $\text{CuO}_x/\text{Pt}/\gamma\text{-Al}_2\text{O}_3$. Previously, our group has reported that supported CuAl_2O_4 exhibits a higher $\text{NH}_3\text{-NO-O}_2$ reaction activity to N_2 compared to supported CuO because supported CuAl_2O_4 exhibits a higher fraction of the Cu^{2+} active species for the reaction.⁴ Therefore, the trend for N_2/NO selectivities over $\text{CuO}_x/\text{Pt}/\alpha\text{-Al}_2\text{O}_3$ and $\text{CuO}_x/\text{Pt}/\text{Al}_2\text{O}_3$ can be explained in a similar manner. Moreover, physically mixed catalysts ($\text{CuO} + \text{Pt}/\text{Al}_2\text{O}_3$, $\text{CuAl}_2\text{O}_4 + \text{Pt}/\text{Al}_2\text{O}_3$ and $\text{CuO}_x/\text{Al}_2\text{O}_3 + \text{Pt}/\text{Al}_2\text{O}_3$) exhibited lower N_2 selectivity at high reaction temperatures (*ca.* > 600 °C) compared to binary catalysts (ESI^\dagger), indicating that highly dispersed Pt and proximate CuO_x particles



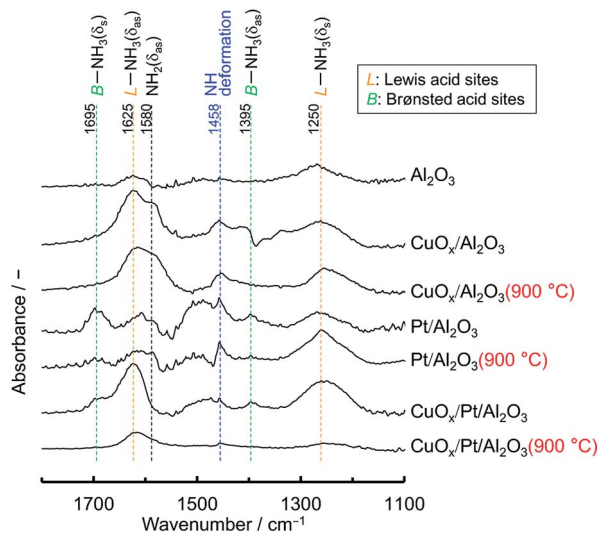


Fig. 6 *In situ* FTIR spectra of NH_3 adsorbed on supports and catalysts before and after thermal aging in air at $900\text{ }^\circ\text{C}$ for 100 h. The spectra were recorded at $200\text{ }^\circ\text{C}$ in gas feeds of 0.3% NH_3 with He balance.

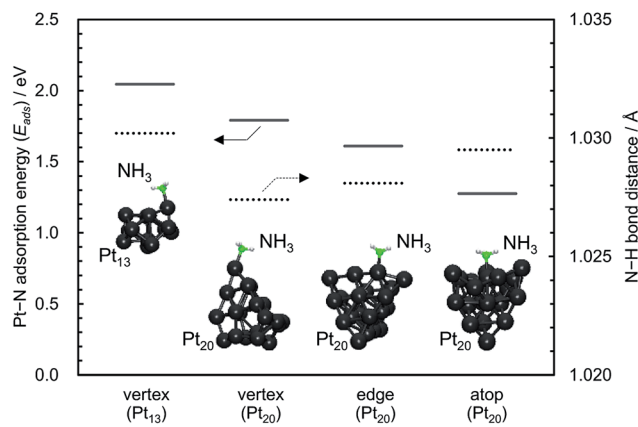


Fig. 7 Adsorption energy (E_{ads}) between NH_3 and Pt_{13} and/or Pt_{20} clusters (Pt-N) and bond distances of N-H in NH_3 adsorbed on Pt_{13} and/or Pt_{20} obtained by the DFT computations.

are required to achieve high N_2 selectivity for catalytic NH_3 combustion. On the other hand, Pt/CuO exhibited high N_2 selectivity, albeit low catalytic activity (ESI \dagger), probably because of low Pt dispersion. To examine the acid and base properties of these catalysts, the amount of desorbed gas per surface area of the catalyst was estimated using NH_3 - and NO-temperature-programmed desorption (TPD) over a range of $50\text{--}500\text{ }^\circ\text{C}$ (ESI \dagger). Table 1 summarises this data. For all catalysts after aging, the amount of desorbed NO increased noticeably, likely because of decreased surface area. However, before and after aging, $\text{CuO}_x/\text{Pt}/\text{Al}_2\text{O}_3$ exhibited relatively higher NH_3 and NO adsorption properties compared to $\text{CuO}/\text{Al}_2\text{O}_3$ and $\text{Pt}/\text{Al}_2\text{O}_3$. These results indicated that $\text{CuO}_x/\text{Pt}/\text{Al}_2\text{O}_3$ exhibits higher acidity and basicity compared to single supported catalysts; therefore, the reactivity of $\text{NH}_3\text{--NO}$ to N_2 is enhanced on the $\text{CuO}_x/\text{Pt}/\text{Al}_2\text{O}_3$ surface.

Finally, the effects of CuO, Cu_2O and metallic Cu on the catalytic NH_3 combustion properties are discussed. ESI \dagger denotes

the comparison of the temperature dependence on the selectivities of the products that were obtained when compared to those of the commercially available CuO, Cu_2O and metallic Cu. The metallic Cu was prepared from CuO that was reduced at $400\text{ }^\circ\text{C}$ for 30 min in 5% H_2/He because CuO can be reduced to metallic Cu at an approximate temperature of $300\text{ }^\circ\text{C}$, as demonstrated from the H_2 -TPR measurement.⁴ For observing the NH_3 combustion activity, the light-off curve for CuO was obtained at approximately $300\text{ }^\circ\text{C}$; further, Cu_2O and metallic Cu exhibited lower activity when compared to that exhibited by CuO. Therefore, it can be considered that CuO (Cu^{2+} oxidation state) acts as an active site during the reaction. However, while considering the selectivities of the products, Cu_2O and metallic Cu exhibited low $\text{N}_2\text{O}/\text{NO}$ selectivities because their activities (NH_3 conversions) were observed to be low. In the O_2 -excess condition for NH_3 combustion ($\lambda = 2.0$), it can be considered that the combustion over CuO_x catalysts proceeds because of redox cycling between CuO and Cu_2O .⁴ Further, the XRD patterns of CuO and Cu_2O before and after the reaction ($\lambda = 2.0$) also indicate redox cycling because the patterns of Cu_2O after the reaction revealed diffraction peaks corresponding to those of CuO (ESI \dagger). In addition, based on our previous studies related to *operando* XAFS, similar redox behaviours could be observed in the supported CuO catalysts ($\text{CuO}_x/\text{SiO}_2$).⁴ Therefore, it can be assumed that the effect of metallic Cu on combustion is negligible.

Conclusions

In this study, binary CuO_x and Pt catalysts supported on 3A2S, Al_2O_3 and SiO_2 suppressed the production of $\text{N}_2\text{O}/\text{NO}_x$ via the catalytic combustion of NH_3 as a carbon-free energy source. Among the binary supported CuO_x and Pt catalysts, sequentially impregnated CuO_x/Pt catalysts tended to exhibit higher activity because Pt nanoparticles were highly dispersed onto each support material without inhibition due to the presence of CuO_x . Compared to sequentially impregnated $\text{CuO}_x/\text{Pt}/3\text{A}2\text{S}$ and $\text{CuO}_x/\text{Pt}/\text{SiO}_2$, $\text{CuO}_x/\text{Pt}/\text{Al}_2\text{O}_3$ exhibited high NH_3 combustion activity, N_2 selectivity, and thermal stability. Before and after aging, $\text{CuO}_x/\text{Pt}/\text{Al}_2\text{O}_3$ was characterised as proximate CuAl_2O_4 and dispersed metallic Pt particles. As the combustion activity was closely associated with the Pt particle size, highly dispersed Pt nanoparticles were thought to play a key role in the low-temperature light-off of NH_3 . For selectivity, the proximate CuAl_2O_4 in $\text{CuO}_x/\text{Pt}/\text{Al}_2\text{O}_3$ enhanced the $\text{NH}_3\text{--NO}$ to N_2 reaction, and the catalyst prevented the dissociative adsorption of NH_3 to NH , which was regarded as an intermediate species obtained during the N_2O production. Therefore, $\text{CuO}_x/\text{Pt}/\text{Al}_2\text{O}_3$ exhibits high N_2 selectivity.

Conflicts of interest

There are no conflicts to declare.

Acknowledgements

This research was supported by JST, PRESTO (JPMJPR1344) and JSPS (18K14326). This work was partly supported by JST-Mirai



Program and the Advanced Characterization Platform of the Nanotechnology Platform Japan sponsored by the Ministry of Education, Culture, Sports, Science and Technology (MEXT), Japan. The XAFS experiments were performed at BL9A with the approval of PF, KEK (Proposal No. 2016G527), and at the BL01B1 of SPring-8 with the approval of JASRI (Proposal No. 2017A1050).

Notes and references

- 1 P. Glarborg, A. Jensen and J. Johnsson, *Prog. Energy Combust. Sci.*, 2003, **29**, 89–113.
- 2 (a) J. Andersson and J. Lundgren, *Appl. Energy*, 2014, **130**, 484–490; (b) Y. Bicer, I. Dincer, C. Zamfirescu, G. Vezina and F. Raso, *J. Cleaner Prod.*, 2016, **135**, 1379–1395; (c) S. Giddey, S. Badwal, C. Munnings and M. Dolan, *ACS Sustainable Chem. Eng.*, 2017, **5**, 10231–10239.
- 3 (a) A. Hayakawa, T. Goto, R. Mimoto, T. Kudo and H. Kobayashi, *Mech. Eng. J.*, 2015, **2**, 14–00402; (b) R. Murai, R. Omori, R. Kano, Y. Tada, H. Higashino, N. Nakatsuka, J. Hayashi, F. Akamatsu, K. Iino and Y. Yamamoto, *Energy Procedia*, 2017, **120**, 325–332.
- 4 (a) S. Hinokuma, *et al.*, *Chem. Lett.*, 2016, **45**, 179–181; (b) S. Hinokuma, *et al.*, *J. Phys. Chem. C*, 2016, **120**, 24734–24742; (c) S. Hinokuma, *et al.*, *J. Phys. Chem. C*, 2017, **121**, 4188–4196; (d) S. Hinokuma, *et al.*, *J. Ceram. Soc. Jpn.*, 2017, **125**, 770–772; (e) S. Hinokuma, *et al.*, *Catal. Commun.*, 2018, **105**, 48–51; (f) S. Hinokuma, *et al.*, *Catal. Today*, 2018, **303**, 2–7; (g) S. Hinokuma, *et al.*, *J. Catal.*, 2018, **361**, 267–277.
- 5 (a) L. Gang, B. Anderson, J. van Grondelle, R. van Santen, W. van Gennip, J. Niemantsverdriet, P. Kooyman, A. Knoester and H. Brongersma, *J. Catal.*, 2002, **206**, 60–70; (b) M. Yang, C. Wu, C. Zhang and H. He, *Catal. Today*, 2004, **90**, 263–267; (c) J. Lee, Y. Lim, B. Park, A. Adelodun and Y. Jo, *Bull. Korean Chem. Soc.*, 2015, **36**, 162–167.
- 6 (a) R. Burch and B. Southward, *J. Catal.*, 2000, **195**, 217–226; (b) R. Burch and B. Southward, *Chem. Commun.*, 2000, 1115–1116; (c) H. Kusar, A. Ersson, M. Vosecky and S. Jaras, *Appl. Catal., B*, 2005, **58**, 25–32; (d) G. Olofsson, A. Hinz and A. Andersson, *Chem. Eng. Sci.*, 2004, **59**, 4113–4123; (e) G. Olofsson, L. Wallenberg and A. Andersson, *J. Catal.*, 2005, **230**, 1–13; (f) M. Sun, S. Wang, Y. Li, Q. Wang, H. Xu and Y. Chen, *J. Taiwan Inst. Chem. Eng.*, 2017, **78**, 401–408; (g) M. Jabłońska, *Catal. Commun.*, 2015, **70**, 66–71.
- 7 S. Lin, A. Gluhoi and B. Nieuwenhuys, *Catal. Today*, 2004, **90**, 3–14.
- 8 M. Lippits, A. Gluhoi and B. Nieuwenhuys, *Catal. Today*, 2008, **137**, 446–452.
- 9 H. Suzuki, M. Shimizu, H. Kamiya, T. Ota and M. Takahashi, *Adv. Powder Technol.*, 1997, **8**, 311–323.
- 10 B. D. Cullity, *Elements of X-RAY DIFFRACTION*, Addison-Wesley Publishing Company, Inc., Philippines, 1978.
- 11 (a) M. Hatanaka, N. Takahashi, T. Tanabe, Y. Nagai, A. Suda and H. Shinjoh, *J. Catal.*, 2009, **266**, 182–190; (b) J. Anderson, R. Daley, S. Christou and A. Efstathiou, *Appl. Catal., B*, 2006, **64**, 189–200; (c) Y. Nagai, T. Hirabayashi, K. Dohmae, N. Takagi, T. Minami, H. Shinjoh and S. Matsumoto, *J. Catal.*, 2006, **242**, 103–109.
- 12 (a) Y. Zhao and D. G. Truhlar, *Theor. Chem. Acc.*, 2008, **120**, 215–241; (b) A. Schäfer, H. Horn and R. Ahlrichs, *J. Chem. Phys.*, 1992, **97**, 2571–2577; (c) D. Andrae, U. Häussermann, M. Dolg, H. Stoll and H. Preuss, *Theor. Chim. Acta*, 1990, **77**, 123–141; (d) R. Ahlrichs, M. Bär, M. Häser, H. Horn and C. Kölmel, *Chem. Phys. Lett.*, 1989, **162**, 165–169; (e) TURBOMOLE, A development of University of Karlsruhe and Forschungszentrum Karlsruhe GmbH, 1989–2007, TURBOMOLE GmbH, since 2007, available from <http://www.turbomole.com>; (f) K. Eichkorn, F. Weigend, O. Treutler and R. Ahlrichs, *Theor. Chem. Acc.*, 1997, **97**, 119–124.
- 13 (a) F. Giordanino, E. Borfecchia, K. Lomachenko, A. Lazzarini, G. Agostini, E. Gallo, A. Soldatov, P. Beato, S. Bordiga and C. Lamberti, *J. Phys. Chem. Lett.*, 2014, **5**, 1552–1559; (b) U. Deka, A. Juhin, E. Eilertsen, H. Emerich, M. Green, S. Korhonen, B. Weckhuysen and A. Beale, *J. Phys. Chem. C*, 2012, **116**, 4809–4818.
- 14 Z. Tian, Y. Li, L. Zhang, P. Glarborg and F. Qi, *Combust. Flame*, 2009, **156**, 1413–1426.
- 15 (a) S. Yang, Y. Liao, S. Xiong, F. Qi, H. Dang, X. Xiao and J. Li, *J. Phys. Chem. C*, 2014, **118**, 21500–21508; (b) Y. Liu, T. Gu, X. Weng, Y. Wang, Z. Wu and H. Wang, *J. Phys. Chem. C*, 2012, **116**, 16582–16592; (c) L. Darvell, K. Heiskanen, J. Jones, A. Ross, P. Simell and A. Williams, *Catal. Today*, 2003, **81**, 681–692; (d) G. Busca, L. Lietti, G. Ramis and F. Berti, *Appl. Catal., B*, 1998, **18**, 1–36; (e) J. Amores, V. Escribano, G. Ramis and G. Busca, *Appl. Catal., B*, 1997, **13**, 45–58; (f) G. Ramis, L. Yi, G. Busca, M. Turco, E. Kotur and R. Willey, *J. Catal.*, 1995, **157**, 523–535; (g) B. Duffy, H. Curryhyde, N. Cant and P. Nelson, *J. Catal.*, 1994, **149**, 11–22.
- 16 (a) V. Dasireddy, B. Likozar and J. Valand, *Appl. Catal., B*, 2018, **237**, 1044–1058; (b) S. Lambert, C. Cellier, P. Grange, J. Pirard and B. Heinrichs, *J. Catal.*, 2004, **221**, 335–346.
- 17 G. Busca, *Catal. Today*, 2014, **226**, 2–13.
- 18 K. Okada, A. Hattori, T. Taniguchi, A. Nukui and R. Das, *J. Am. Ceram. Soc.*, 2000, **83**, 928–932.
- 19 M. Ferrandon, B. Ferrand, E. Bjornbom, F. Klingstedt, A. Neyestanaki, H. Karhu and I. Vayrynen, *J. Catal.*, 2001, **202**, 354–366.

